JOURNAL OF MATERIALS SCIENCE 15 (1980) 959–973

δ-FeO(OH) and its solutions

Part 3 *A study of the thermal decomposition*

OLAF MULLER, ROBERT WILSON*, HENDRIK COLIJN, WILLIAM KRAKOW†
Xerox Corporation, Xerox Square, W114, Rochester, New York 14644, USA

Decomposition products of δ-FeO(OH)-type $Fe_{1-x}M_xO_{1-x}(OH)_{1+x}$ phases (M = Mg, Zn, Ca, Cd) have been studied by X-ray diffraction, electron diffraction and high-resolution transmission electron microscopy. It has been shown that the M = Mg and Cd δ-phases decompose to α-Fe_2O_3-based solid solutions which in turn undergo exsolution to form some MgO and CdO at a higher temperature. In the case of $Fe_{1-x}Zn_xO_{1-x}(OH)_{1+x}$, the decomposition proceeds over α-Fe_2O_3 ss to an unstable spinel solid solution. All decomposition products are topotactically related to their precursors in the decomposition chain. In the electron microscope some δ-type phases undergo *in situ* decomposition under intense beam bombardment with somewhat different results than obtained for thermal decomposition products under ambient conditions. The plate-like morphology and crystal size is retained in the decomposition products; however, the products have a more pitted appearance after decomposition.

1. Introduction

In Part 1 of this series [23] we discussed the preparation and crystal chemistry of δ-FeO(OH)-type solid solutions of composition $Fe_{1-x}M_xO_{1-x}(OH)_{1+x}$ where M = Mg, Zn, Cd and Ca. In Part 2 [24] we have dealt with the structural and morphological characteristics of the unsubstituted δ-FeO(OH) which was thoroughly investigated by high-resolution transmission electron microscopy.

Although a number of papers [1–14] have already treated the thermal decomposition of unsubstituted δ-FeO(OH), no such study is available on substituted δ-FeO(OH)-type phases. In this part we will give an X-ray and TEM study of the thermal decomposition of δ-type $Fe_{1-x}M_xO_{1-x}(OH)_{1+x}$ where M = Mg, Zn, Cd and Ca, with an emphasis on phases with M = Mg and Zn.

The thermal decomposition of δ-FeO(OH) has been studied by numerous techniques including X-ray diffraction, DTA, TGA, TEM, and Mössbauer spectroscopy [1–14]. There are numerous discrepancies in the literature on this subject‡ since the decomposition process apparently depends on the size, crystallinity, heating rate, and method of preparation of δ-FeO(OH). Most δ-FeO(OH) products start to lose water on prolonged heating above 80° C. At first there is no drastic change in crystal structure. Some authors [8, 9] even claim that δ-FeO(OH) can be completely dehydrated (to "δ-Fe_2O_3") by heating beyond 120° C without change in structure. However, this claim is contradicted by others [1, 2]. For very fine, poorly crystallized δ-FeO(OH), the decomposition (in air) proceeds directly to α-Fe_2O_3, while for coarser, better crystallized materials, the δ-phase converts partly to anion-deficient α-FeO(OH) before finally decomposing to α-Fe_2O_3 [1, 4]. There is general agreement that on reaching 220 to 240° C, δ-FeO(OH) has converted to a poorly crystallized, disordered α-Fe_2O_3. On going to still higher temperatures, the latter product becomes more

* Present address: Pennsylvania State University, University Park, Pennsylvania 16802, USA.
† Present address: IBM Corporation, Thomas J. Watson Research Center, P.O. Box 218, Yorktown Heights, New York 10598, USA.
‡ Such discrepancies are discussed in [13].

0022–2461/80/040959–15$03.50/0

ordered and better crystallized. It has been claimed [7] that certain δ-FeO(OH), α-FeO(OH) composites decompose first to a hydrated α-Fe_2O_3 ($Fe_2O_3 \cdot 0.5H_2O$) before completely losing the water at higher temperatures. Under some conditions, δ-FeO(OH) can convert completely to α-FeO(OH); e.g. when subjecting the very coarse δ-phase to 200° C for 30 min [4], on heating an alkaline δ-FeO(OH) suspension at 75 to 80° C [5, 7] or by hydrothermal conversion above 100° C [1].

In a recent study [14] it is concluded that the α-FeO(OH) derived from the δ-phase is never completely identical with well-crystallized α-FeO(OH). It is therefore best to label it α'-FeO(OH) and to consider it as a transitional stage in the crystalline order between δ-FeO(OH) and pure α-FeO(OH). The δ-FeO(OH) → α-FeO(OH) → α-Fe_2O_3 conversion is topotactic [1–5] as the hexagonally close-packed anion layers are retained, but the Fe atoms become progressively more ordered with increasing temperature. Even in the first stage of decomposition of δ-FeO(OH) there is evidence of a structural equilization of the two magnetic sublattices, as seen from the Mössbauer spectra and lower magnetization values [12]. The so-called "δ-Fe_2O_3" phase is thus considered an intermediate stage toward the formation of a fully ordered α-Fe_2O_3 [12]. In a dehydration study of larger α-FeO(OH) crystals by X-ray and electron diffraction [15], satellite reflections reveal an intermediate state which can be interpreted as a sinusoidal structure–amplitude modulation along the *c*-axis of α-Fe_2O_3 corresponding to a repeat distance of 32 Å.

In spite of the voluminous literature on the δ-FeO(OH) decomposition process, the structural changes taking place are only known superficially and have not yet been probed in detail by single-crystal electron diffraction. Moreover, most of the electron micrographs of such decomposition products [6, 13, 16] are only survey pictures with only rare glimpses of greater morphological detail such as found in [14]. To our knowledge, thermal decomposition studies of δ-type $Fe_{1-x}M_xO_{1-x}(OH)_{1+x}$ phases have not yet been carried out. It is the purpose of the present study to fill these gaps and to probe the topotactic relationships between the δ-type precursor and the decomposition products.

2. Experimental procedure

The preparation of the $Fe_{1-x}M_xO_{1-x}(OH)_{1+x}$ starting materials has been described in Part 1 and will not be repeated here.

Decomposition studies of most materials were carried out by oven heating the $Fe_{1-x}M_xO_{1-x}(OH)_{1+x}$ samples in air for 5 days at various temperatures, as shown in Table I for selected examples. For that purpose, the samples were loosely wrapped in Al or Pt foils, depending on whether the decomposition took place at low or high temperatures. Some samples were also examined by TGA in air at 20° C min^{-1}.

After heating, all samples were examined by X-ray diffraction methods using a Siemens diffractometer with Cu$K\alpha$ radiation and glass slide mounts. Single-phase products were further characterized by internally standardized slow scan diffractometer traces to derive accurate cell parameters.

The TEM techniques used were the same as those described in Part 2 and will not be repeated here. However, electron diffraction experiments which have not been described previously require additional consideration. In these experiments a 10 μm field-limiter aperture was employed which included areas < 2000 Å in diameter. This produced a slight broadening of the Bragg reflections because of the diffraction limit of the post specimen aperture, but still allowed sufficiently high-resolution diffraction detail to be observed for structural identification. One further point which requires consideration was that thin carbon films < 50 Å were employed to minimize their contribution to the scattering. Furthermore, a goniometer stage was often employed to optimize the scattering from individual crystalline particles such that Bragg reflections of the same diffraction order were equally excited.

3. Results and discussion

3.1. Overall picture

The X-ray results of our decomposition studies are summarized in Table I. The systems $Fe^{3+}_{1-x}M^{2+}_xO_{1-x}(OH)_{1+x}$ with $M = Mg^{2+}$ and Zn^{2+} have been most intensively studied and their decomposition scheme is represented in Fig. 1. Although X-ray diffraction has been used primarily to interpret the decomposition process, the X-ray peaks of many of the decomposition products were so weak and diffuse that an unambiguous interpretation was difficult or impossible. It was therefore important to supplement our data with TEM and single-crystal electron diffraction data not only to

TABLE I Thermal decomposition products of δ-type $Fe_{1-x}M_xO_{1-x}(OH)_{1+x}$ solid solutions, M = Mg, Zn, Ca, Cd

M	x	Temperature (° C) of 5 day heat treatment	X-ray results
Mg	0	110	δ-FeO(OH) → α-Fe_2O_3
Mg	0	155	α-Fe_2O_3, very diffuse 1 0 4 peak
Mg	0	260	α-Fe_2O_3, diffuse 1 0 4 peak
Mg	0	830	α-Fe_2O_3, sharp 1 0 4 peak
Mg	0.17	110	δ-FeO(OH) → α-Fe_2O_3
Mg	0.17	155	α-Fe_2O_3 ss, very diffuse 1 0 4 peak
Mg	0.17	260	α-Fe_2O_3 ss, diffuse 1 0 4 peak
Mg	0.17	430	α-Fe_2O_3 ss, better crystallized
Mg	0.17	830	α-Fe_2O_3 + spinel phase
Mg	0.27	110	δ-FeO(OH) → α-Fe_2O_3
Mg	0.27	155	α-Fe_2O_3 ss, very diffuse 1 0 4 peak
Mg	0.27	320	α-Fe_2O_3 ss
Mg	0.27	430	α-Fe_2O_3 ss + possible trace of MgO ss
Mg	0.27	830	α-Fe_2O_3 + spinel phase
Mg	0.43	110	δ-FeO(OH) ss, extremely poor crystallinity
Mg	0.43	155	δ-FeO(OH) → α-Fe_2O_3
Mg	0.43	210	α-Fe_2O_3 ss, extremely poor crystallinity
Mg	0.43	320	α-Fe_2O_3 ss + trace of MgO ss
Mg	0.43	430	α-Fe_2O_3 ss + MgO ss
Mg	0.43	830	Spinel phase + probable MgO ss
Mg	0.63	110	Green rust I + δ-FeO(OH) ss
Mg	0.63	155	Unidentified phase(s)
Mg	0.63	210	Nearly amorphous material
Mg	0.63	430	α-Fe_2O_3 ss + MgO ss
Mg	0.63	830	Spinel phase + MgO
Mg	0.83	210	$Mg(OH)_2$ ss, reduced unit cell
Mg	0.83	260	$Mg(OH)_2$ ss + Fe_2O_3 ss
Mg	0.83	320	MgO (very poorly crystallized) + α-Fe_2O_3 ss
Mg	0.83	430	MgO ss + α-Fe_2O_3 ss
Zn	0.11	110	δ-FeO(OH) → α-Fe_2O_3
Zn	0.11	155	α-Fe_2O_3 ss + trace of α-FeO(OH)
Zn	0.11	210	α-Fe_2O_3 ss
Zn	0.11	260	α-Fe_2O_3 ss
Zn	0.11	320	α-Fe_2O_3 ss + small amount of spinel
Zn	0.11	830	α-Fe_2O_3 + spinel
Zn	0.22	110	δ-FeO(OH) → α-Fe_2O_3
Zn	0.22	155	α-Fe_2O_3 ss
Zn	0.22	260	α-Fe_2O_3 ss
Zn	0.22	320	α-FeO_3 ss + spinel
Zn	0.22	830	α-Fe_2O_3 + spinel
Zn	0.33	110	δ-FeO(OH) → α-Fe_2O_3
Zn	0.33	155	α-Fe_2O_3 ss, very poor crystallinity
Zn	0.33	210	Spinel + α-Fe_2O_3 ss
Zn	0.33	260	Mostly spinel + small amount of α-Fe_2O_3 ss
Zn	0.33	320	Spinel
Zn	0.33	430	Spinel
Zn	0.33	830	Spinel + trace of α-Fe_2O_3
Zn	0.45	110	δ-FeO(OH) → α-Fe_2O_3 + ZnO
Zn	0.45	155	α-Fe_2O_3 ss + possible trace of ZnO and spinel
Zn	0.45	210	Spinel + small amount of α-Fe_2O_3 ss + ZnO
Zn	0.45	260	Spinel + small amount of ZnO and trace of α-Fe_2O_3 ss
Zn	0.45	830	Spinel + small amount of ZnO
Ca	0.10	110	δ-FeO(OH) → α-Fe_2O_3
Ca	0.10	155	α-Fe_2O_3 ss
Ca	0.10	210	α-Fe_2O_3 ss
Ca	0.10	830	α-Fe_2O_3 + $CaFe_2O_4$
Cd	0.12	210	α-Fe_2O_3 ss, diffuse 1 0 4 peak

TABLE I (*continued*) . . .

M	x	Temperature (° C) of 5 day heat treatment	X-ray results
Cd	0.12	320	α-Fe_2O_3 ss
Cd	0.12	380	α-Fe_2O_3 ss + trace CdO
Cd	0.34	210	α-Fe_2O_3 ss, very diffuse peaks
Cd	0.34	260	α-Fe_2O_3 ss + trace CdO
Cd	0.34	320	α-Fe_2O_3 ss + CdO
Cd	0.34	440	CdO + α-Fe_2O_3 ss + spinel

confirm the X-ray diffraction record but also to give us new insights into the decomposition process and the topotactic relationship between the various phases in the decomposition chain. TEM and electron diffraction are more dynamic methods than XRD, permitting us to probe very small volumes of crystalline material at a very high real-space and reciprocal-space resolution.

Below we will discuss separately the decomposition process for the substituted δ-phases of the type $Fe_{1-x}M_xO_{1-x}(OH)_{1+x}$ with M = Mg, Zn, Cd and Ca. The last two systems (M = Cd, Ca) have only been superficially studied and will only be treated briefly.

3.2. The thermal decomposition of $Fe_{1-x}Mg_xO_{1-x}(OH)_{1+x}$

The Mg-substituted δ-phases all decompose first to an α-Fe_2O_3-type solid solution, as seen from Table I and Fig. 1. In our study we did not detect any α-FeO(OH) products which is probably due to the very finely divided state of the samples and the long (5 day) heat treatment.

The phase labelled in Table I as δ-FeO(OH) → α-Fe_2O_3 can be described as having an X-ray powder pattern like δ-FeO(OH) with the addition of a diffuse high-intensity region at the 1 0 4 peak position of the α-Fe_2O_3 pattern. We interpret this as the first sign of rudimentary transition of the δ-phase toward α-Fe_2O_3 or a corundum structure. As the temperature is increased further, this high-intensity region transforms into a very broad and weak 1 0 4 α-Fe_2O_3 peak, as is illustrated in Fig. 2b for the 17% Mg substituted δ-phase. The trace given in Fig. 2b can already be indexed on the basis of the α-Fe_2O_3 unit cell, although the peaks (such as the 1 0 4) which distinguish the α-Fe_2O_3 phase from the δ-phase, are still extremely weak and broad due to the very poorly ordered state of the Fe atoms in the newly formed α-Fe_2O_3 structure. It is possible that this phase is composed of small islands of a α-Fe_2O_3-like areas in a more disordered matrix. The 1 0 0 and 1 0 1 δ-peaks transform to the 1 1 0 and 1 1 3 peaks of α-Fe_2O_3 in accord with the previously described topotactic relationship between δ-FeO(OH) and α-Fe_2O_3 [1].

At still higher temperatures, the α-Fe_2O_3 phase becomes better crystallized as the 1 0 4 peak

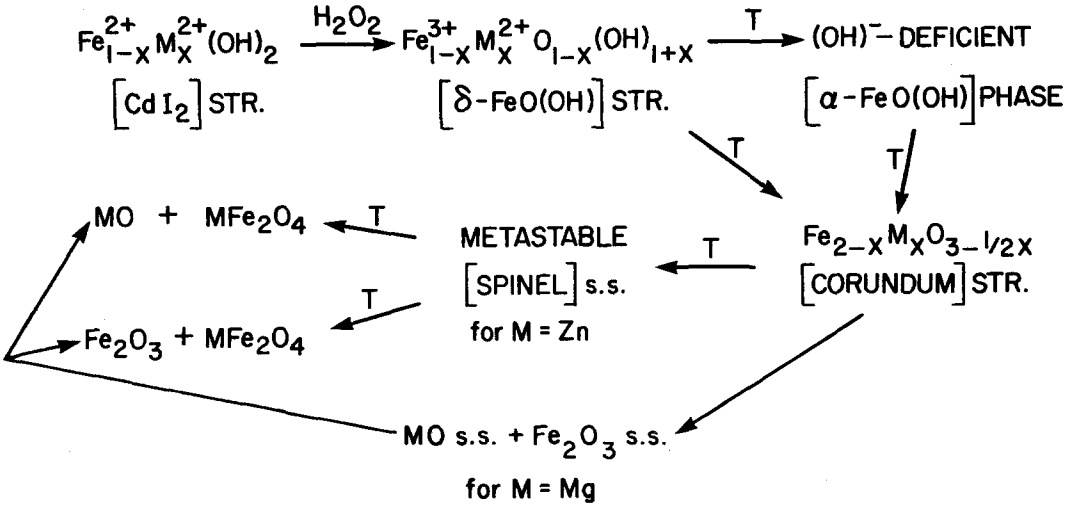

Figure 1 Schematic diagram, illustrating the formation and thermal decomposition of δ-type $Fe_{1-x}M_xO_{1-x}(OH)_{1+x}$ solid solutions with M = Zn and Mg.

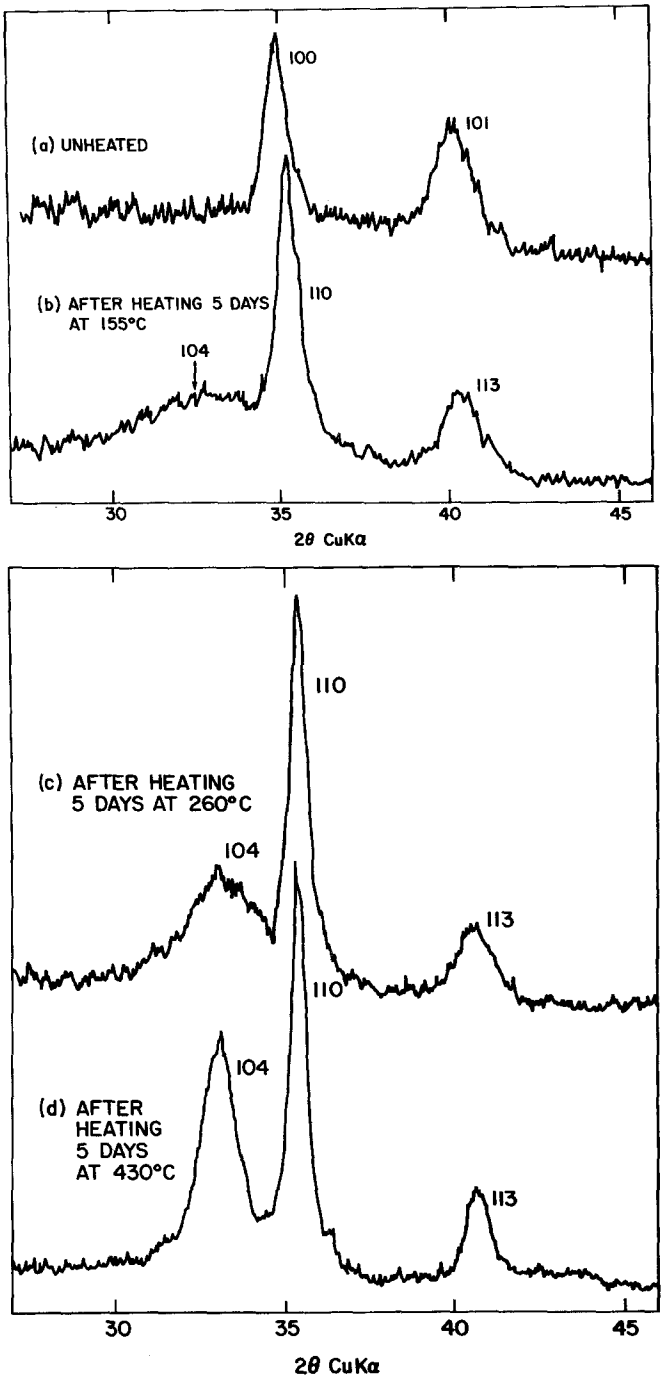

Figure 2 X-ray diffraction trace of (a) δ-type $Mg_{0.17}Fe_{0.83}O_{0.83}(OH)_{1.17}$ and (b) its decomposition product at 155° C, a highly disordered α-Fe_2O_3-type solid solution. (c) Same material decomposed at 260° C, and (d) at 430° C showing progressively higher degrees of order in the α-Fe_2O_3-type structure.

becomes progressively sharper as illustrated in Fig. 2c and d. After heating for 5 days at 430° C, the Fe atoms have now become well ordered. However, the 1 0 4 peak (and the other $h\,k\,l$ peaks with $l \neq 0$) are still not as sharp as the $h\,k\,0$ peaks, due to line broadening caused by the thin nature of the hexagonal platelets of the δ-FeO(OH)-type precursor along the c-axis and due to the fact that the heat treatment at 430° C was not sufficient to cause sintering. However, after a 5 day heat treatment at 830° C, the α-Fe_2O_3 phase sinters and becomes uniformly well crystallized with the 1 0 4 peak now becoming the most intense of the X-ray pattern.

The question can be asked whether or not the α-Fe_2O_3-type phases shown in Table I and Fig. 2 are completely dehydrated or retain some hydroxide ions. To answer that question, TGA

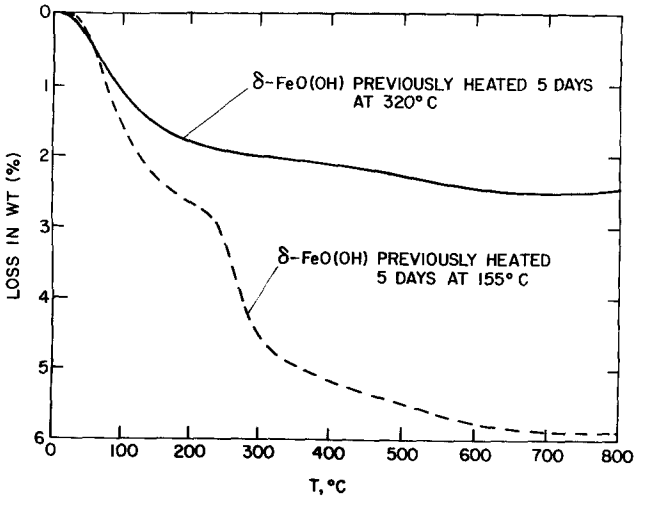

Figure 3 TGA traces for δ-FeO(OH) previously decomposed at 155 and 320° C. Heating rate: 20° C min^{-1} in air.

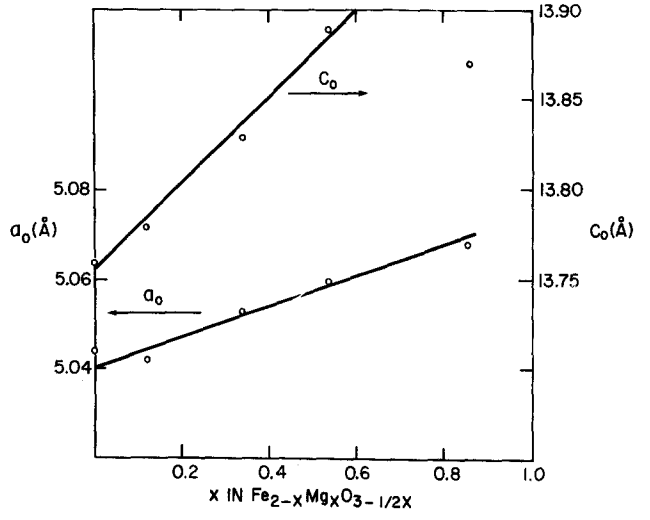

Figure 4 Hexagonal unit cell parameters of α-Fe_2O_3-type $Fe_{2-x}Mg_xO_{3-1/2x}$ as a function of composition.

traces were obtained for a number of decomposition products. In Fig. 3, two such traces are shown of δ-FeO(OH) which had previously been converted to α-Fe_2O_3 by heating for 5 days at 320 and 155° C. We can see that the sample previously heated at 320° C has lost only about 2 wt% adsorbed water* and heating to higher temperatures does not result in any significant additional weight loss. This sample can therefore be considered to be anhydrous. However, the material previously heated at 155° C shows not only the loss of adsorbed water but also the expulsion of additional water at a higher temperature amounting to almost 3%. This additonal water is apparently structurally held as hydroxide. Similar traces were observed for other substituted phases indicating that some structural water is still present for the low-temperature α-Fe_2O_3-type dehydration products ($T = 155°$ C), but that such water is lost at higher temperatures.

It has been shown previously that the cell parameters of δ-type $Fe_{1-x}M_xO_{1-x}(OH)_{1+x}$ phases increase with increasing x.† A similar trend occurs for the α-Fe_2O_3-type dehydration products as illustrated in Fig. 4 for the $Fe_{2-x}Mg_xO_{3-1/2x}$ system prepared at 320° C. The unit cell volumes obtained from Fig. 4 are slightly smaller than the nine-fold increase expected from the known topotactic relationship between α-Fe_2O_3 and δ-FeO(OH) [1]. This is also evident from the shift in peak positions in Fig. 2 and can be attributed to the loss of anions in this structural

* The high adsorbed water content cannot be avoided during handling under ambient conditions due to the very finely divided state of these products.
† See Table I Part 1 [23].

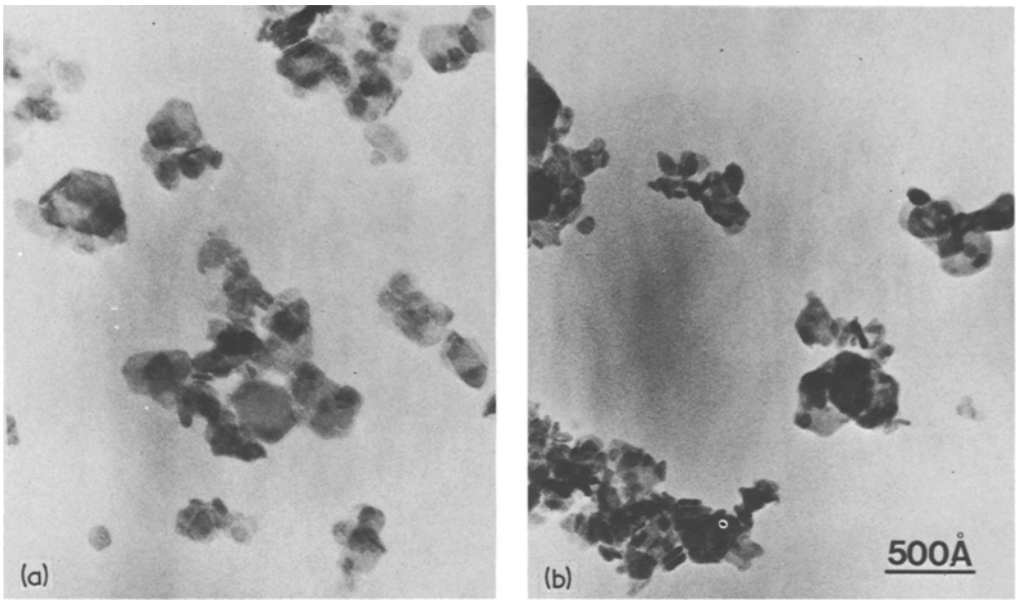

Figure 5 Bright-field transmission electron micrograph of $Fe_{0.73}Mg_{0.27}O_{0.73}(OH)_{1.27}$ crystallites (a) unheated and (b) heated for 5 days at 210° C.

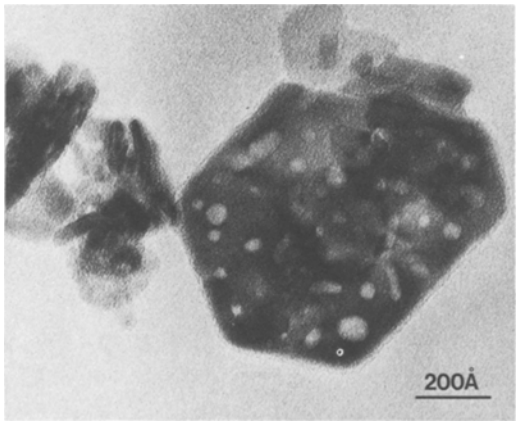

Figure 6 Micrograph of the same material shown in Fig. 5b but at a higher magnification.

transformation. In Fig. 4 the points plotted at $x = 0.86$ probably already correspond to a two-phase mixture, although the second phase could not be detected by X-rays.

As seem from Fig. 5, the Mg-substituted δ-phases have the same general appearance before and after conversion to the α-Fe_2O_3 structure, indicating that particle size and shape are retained through the conversion. However, on closer inspection at higher magnification (Fig. 6), the TEM micrographs show the presence in some particles of large pores or material deficient areas which were not observed before dehydration. The surfaces of the δ-particles are pitted on a finer level as shown in Parts 1 and 2. A similar coarsening of the surface structure has been observed for unsubstituted δ-FeO(OH) after heating in air at 200° C [14]. This has been attributed to the expulsion of water when H^+ ions migrate toward the surface of the δ-particles and combine with OH^- ions to form water which can escape by moving along channels and pores and widening the pores. At the same time, the Fe atoms rearrange themselves into more stable positions, yielding eventually well-ordered α-Fe_2O_3 [14]. Our observations on substituted δ-phases are not in conflict with this hypothesis.* It should be pointed out that much of the pore volume could be created by the small decrease in cell volume imposed by the topotactic dehydration of the δ-phases; i.e. the mass loss occurs in localized areas rather than by uniform shrinkage of the entire crystallite.

From observing Fig. 1 and Table I, several trends are evident in the decomposition chain of the δ-type $Fe_{1-x}Mg_xO_{1-x}(OH)_{1+x}$. In the initial decomposition, the higher the Mg content the poorer the crystallinity of the α-Fe_2O_3-type solid solutions and the lower the thermal stability

* The observations in [14] differ in detail from our own and others, due in part to structural differences in the δ-structure attributable to differences in the methods of preparation.

toward further decompositions to MgO solid solution and an α-Fe_2O_3 solid solution of lower Mg content. This decomposition chain is made up of a series of phases which are probably thermodynamically unstable and are formed only because each is topotactically related to its precursor. However, at very high temperatures the thermodynamically stable phase assemblages are finally formed: nearly stoichiometric $MgFe_2O_4$, α-Fe_2O_3 and MgO.

When we go to higher Mg contents, the decomposition products are more difficult to interpret since the precursors are probably two-phase mixtures in most of the composition range (see Fig. 1, Part 1 [23]). For $x = 0.63$, the X-ray data of the 155° C decomposition product could not be interpreted while at 210° C, the material was very nearly amorphous with the possible beginning of very diffuse α-Fe_2O_3-type peaks. For $x = 0.83$, a single phase $Mg(OH)_2$ solid solution persisted at 210° C with reduced unit cell parameters. For the same material heated at 260° C, some exsolution of α-Fe_2O_3 ss has taken place but the $Mg(OH)_2$ structure still persists. This is not unexpected in view of a recent study [17] which shows that $Mg(OH)_2$ can retain its structure even when the dehydration process has proceeded quite far.

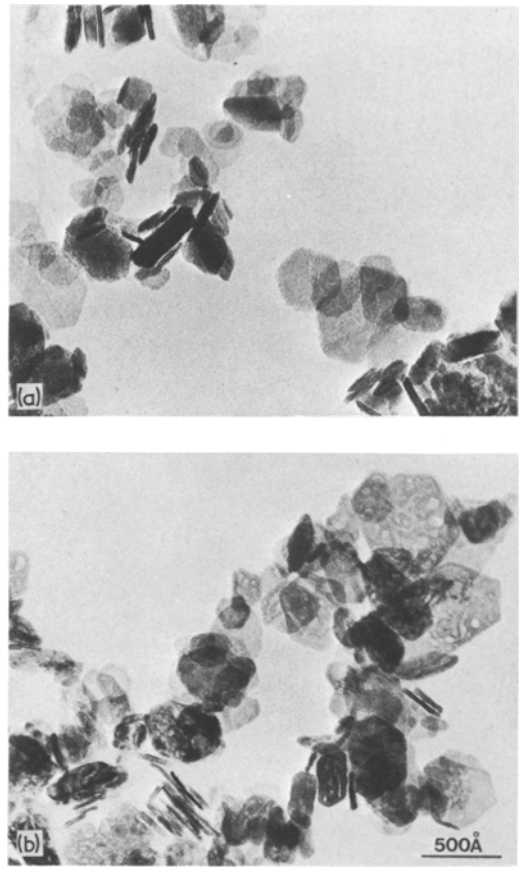

Figure 7 Bright-field micrographs of $Fe_{0.89}Zn_{0.11}O_{0.89}(OH)_{1.11}$ (a) unheated, and (b) previously heated for 5 days at 210° C.

3.3. The thermal decomposition of $Fe_{1-x}Zn_xO_{1-x}(OH)_{1+x}$

As can be seen from Table I and Fig. 1, the thermal decomposition of the $Fe_{1-x}Zn_xO_{1-x}(OH)_{1+x}$ δ-phases proceeds along a slightly different route than for the Mg-analogues. An α-FeO(OH)-type intermediate was only observed rarely and then only as a trace for the 11% Zn substituted material heated to 155° C. We encounter again metastable α-Fe_2O_3-type solid solutions with enlarged unit cells which have the same appearance as their precursors except for the formation of large pores or surface features (Fig. 7). Electron diffraction powder data for these 11% Zn-substituted phases are shown in Fig. 8 confirming the X-ray diffraction record (Table I) and showing that these phases are stable under the conditions of high-vacuum electron beam bombardment.

The Zn-substituted α-Fe_2O_3 solid solutions are thermally less stable toward further decomposition than the Mg-analogues, as is seen from Table I. The decomposition proceeds over metastable spinel-type intermediates of varying stoichiometry* before the stable phase assemblages are finally formed at the highest (830° C) temperatures. This sequence of decomposition reactions can be followed by single-crystal electron diffraction and TEM since the Zn-substituted δ-type phases occur in larger crystallites. Such data are presented in Figs. 9 and 10.

In Fig. 9 we show a bright-field (a) and dark-field (b) electron micrograph of a relatively large $Fe_{0.67}Zn_{0.33}O_{0.67}(OH)_{1.33}$ particle which had been previously heated to 210° C for 5 days. We note that the hexagonal morphology of the δ-type precursor is retained in this decomposition product.

* For most compositions the stoichiometry of this spinel phase is difficult to pinpoint since this phase occurs together with α-Fe_2O_3 solid solutions of varying stoichiometry and the ratio of the two changes with decomposition temperature and Zn content. Some indications of these changes are given by the different ratios of the two co-existing phases and the variations in the *d*-spacings.

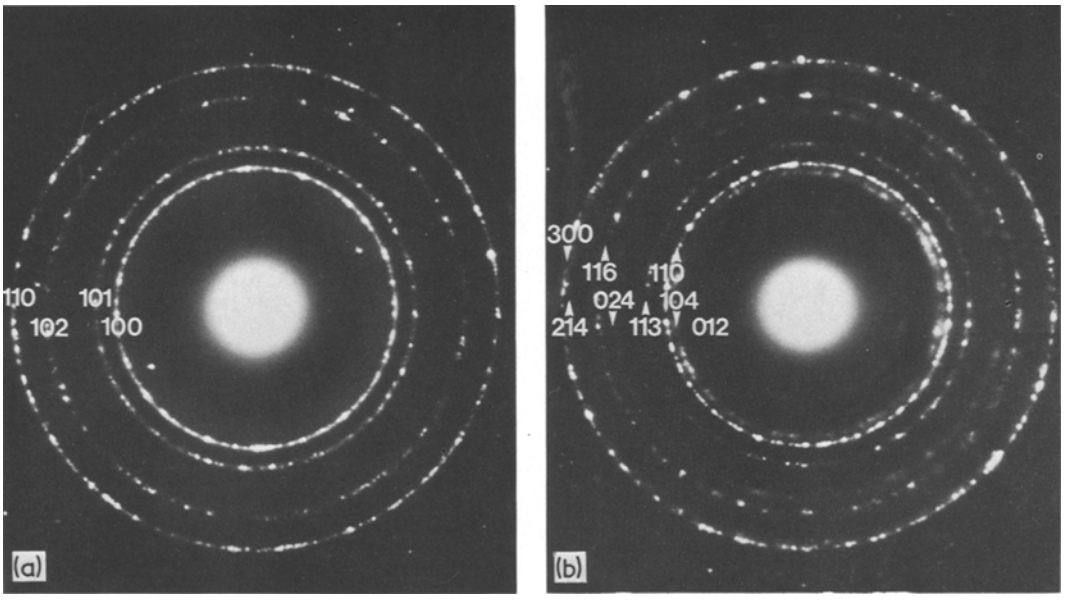

Figure 8 Electron diffraction powder patterns of (a) material in Fig. 7a showing δ-FeO(OH) structure and (b) material in Fig. 7b showing α-Fe_2O_3 (corundum-type) structure.

The corresponding electron diffraction pattern (Fig. 9c) shows a composite of two single-crystal diffraction patterns: a (0 0 1) projection of an α-Fe_2O_3 ss (corundum structure) superimposed on a (1 1 1) projection of the spinel type. These two hexagonal networks are oriented at 30° angles with respect to each other. From the dark-field picture (Fig. 9b) we can see that selecting a single diffraction spot produces an image from one of the two above-mentioned phases. Therefore, this spotty image can be attributed to compositional and structural differences between small (50 to 100 Å) areas within the larger crystal. Such inhomogeneities are not unexpected since they have also been found for the undecomposed δ-phase (see Part 2).

The decomposition sequence of a 33% Zn-substituted δ-phase is more fully illustrated in Fig. 10 where single-crystal electron diffraction patterns are compared for the unheated material (a), and two samples previously heated to higher temperatures (b and c). All three diffraction patterns were taken on isolated single crystals similar in appearance to Fig. 9a. The pattern of the unheated material could be indexed either on the basis of an undecomposed δ-phase or an α-Fe_2O_3 ss type unit cell since one cannot distinguish between the two possibilities on the basis of the $hk0$ pattern.* From numerous observations we have found that δ-type $Fe_{1-x}Zn_xO_{1-x}(OH)_{1+x}$ materials and their derivatives with $x > 0.20$ tend to decompose gradually under intense electron beam bombardment†; hence the pattern shown in Fig. 10a can be either that of an undecomposed δ-structure or a product converted to the α-Fe_2O_3-type by electron beam bombardment or a composite of both.

The single-crystal electron diffraction pattern in Fig. 10b is similar to Fig. 9a and is a composite of an α-Fe_2O_3 ss and a spinel lattice with the two hexagonal arrays rotated 30° with respect to each other. In Fig. 10b, some of the α-Fe_2O_3-type diffraction spots have been indexed. As the decomposition proceeds further (by heating to 260° C) the α-Fe_2O_3 spots become weaker and the spinel pattern becomes stronger as seen from Fig. 10c where the spinel lattice is indexed. We see that both phases occur in the same single crystal to varying degrees depending on the heat treatment. It is obvious that we have a topotactic reaction mechanism whereby the [0 0 1] axis of the δ-structure becomes the [0 0 1] axis of the α-Fe_2O_3

* As has been pointed out before, the δ-type 1 0 0 and the α-Fe_2O_3 1 1 0 reflections are nearly coincident in their *d*-spacings and intensities.

† The δ-phases with lower Zn concentrations are much more resistant toward such decomposition as seen from Fig. 8a.

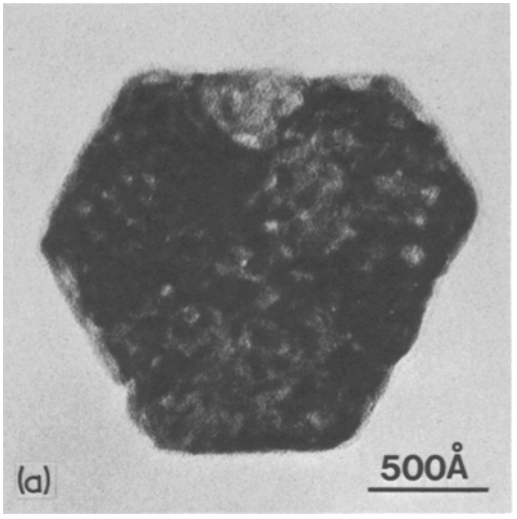

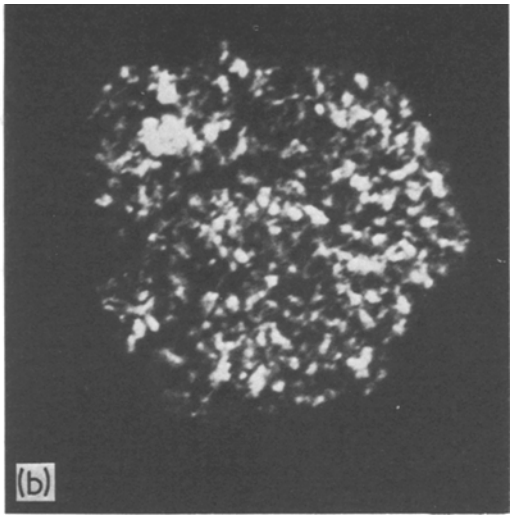

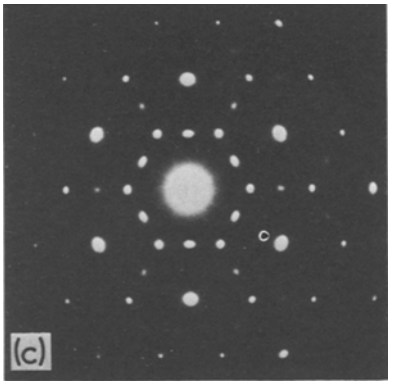

Figure 9 (a) Bright-field and (b) dark-field image of a $Fe_{0.67}Zn_{0.33}O_{0.67}(OH)_{1.33}$ crystal previously decomposed at 210° C for 5 days, and (c) single-crystal electron diffraction pattern of same particle.

or corundum-type which in turn transforms into the [1 1 1] axis of the spinel structure. Similarly, the [1 0 0] of α-Fe_2O_3 is aligned parallel to the [1 $\bar{1}$ 0] of the cubic spinel structure. Overall, the sequence represented in Fig. 10 is in good accord with the X-ray diffraction record of Table I. The electron diffraction records of Fig. 10b and c were taken on particles which had been previously decomposed. It is believed that in this case further decomposition due to electron beam bombardment did not occur since minimum beam dose precautions were applied.

In the α-$Fe_2O_3 \rightarrow$ spinel transformation, the direction along which the anion layers are packed does not change, although we go from hexagonal close-packing in the α-Fe_2O_3-type to a cubic close-packing in the spinel structure. However, in the conversion to the spinel structure, one-third of the cations must migrate from octahedral to tetrahedral sites. This is more easily accomplished for Zn^{2+} ions due to their low octahedral preference – hence

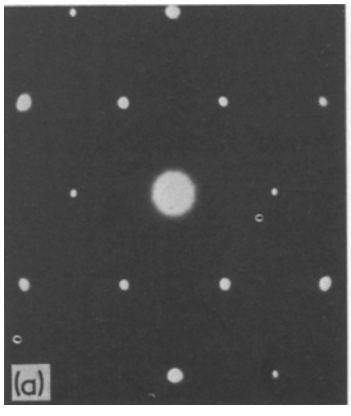

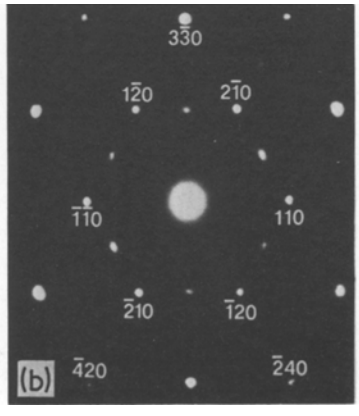

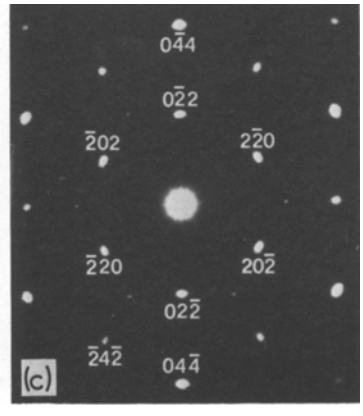

Figure 10 Inner rings of single-crystal electron diffraction patterns of an $Fe_{0.67}Zn_{0.33}O_{0.67}(OH)_{1.33}$ particle (a) unheated, (b) previously heated at 210° C for 5 days, and (c) previously heated at 260° C for 5 days.

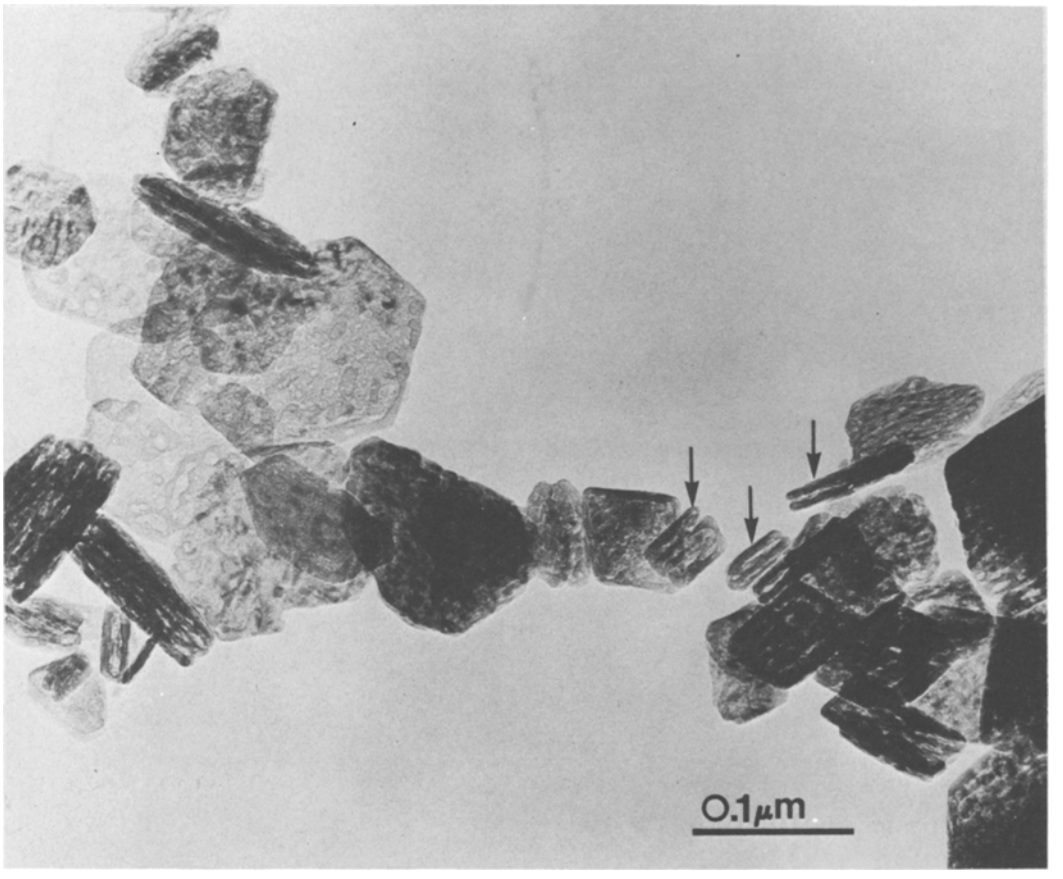

Figure 11 Bright-field micrograph of $Fe_{0.55}Zn_{0.45}O_{0.55}(OH)_{1.45}$ particles previously heated at 260° C for 5 days. Arrows point to some multiply cemented particles.

the easy low-temperature conversion to spinel for the Zn-rich phases.

The same topotactic transformation has been found before in the relationship between α-Fe_2O_3 and spinel-type Fe_3O_4 as shown by electron diffraction [18] and pole figures derived from X-ray data [19, 20]. A similar relationship was found in the orientation of segregated $Fe_{2-x}Mn_xO_3$ in spinel crystals of composition $Mn_{0.78}Fe_{2.22}O_4$ [21].

When we go to still higher Zn concentrations, the decomposition products are even more complex. Both the hexagonal and irregularly shaped crystallites are shown in Fig. 11 for a 45% Zn-substituted δ-phase heated previously to 260° C for 5 days. Again large pore spaces are visible and we see that some of the thin plates have been cemented together into multiples (indicated by arrows in Fig. 11) in a process similar to that described for pure δ-crystallites (see Part 2). Single-crystal electron diffraction patterns of such plates (Fig. 12) show, in addition to the previously described spinel and α-Fe_2O_3-type patterns, a new pattern which has been identified as belonging to hexagonal ZnO. All three phases are topotactically related with the *c*-axes of ZnO and α-Fe_2O_3 ss parallel to the spinel [1 1 1] axis. In all three structures the direction of stacking of the close-packed anion layers is maintained. From Fig. 12 we see that the *b*-axis of ZnO coincides with the $[\bar{1}\,\bar{1}\,0]$ direction of the α-Fe_2O_3-type lattice.

It should be mentioned that we found evidence of some inhomogeneity between different crystals. For example, we have examined other particles with the same overall composition and heat treatment as that for which the diffraction pattern is given in Fig. 12. We find that in some cases the α-Fe_2O_3-type pattern is completely absent. Such differences can be explained in terms of compositional variations between individual crystallites. On the other hand, it is also possible that the individual particles are chemically homogeneous but that the decomposition process has proceeded

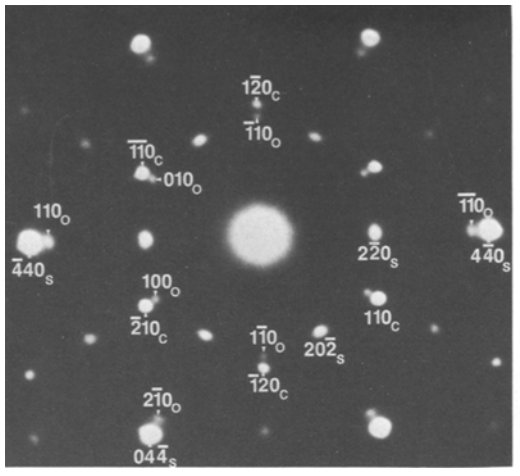

Figure 12 Electron diffraction pattern of a $Fe_{0.55}Zn_{0.45}O_{0.55}(OH)_{1.45}$ particle previously heated for 5 days at 260° C. Subscripts to the Miller indices refer to the different phases: s = spinel, o = ZnO, and c = α-Fe_2O_3 (corundum structure).

at a slower rate in some particles due to such factors as crystal size, morphology, etc.

As mentioned before, the Zn-rich δ-phases are unstable under intense electron beam bombardment and tend to decompose. In Fig. 13, we give an electron diffraction pattern of a previously unheated δ-type $Fe_{0.55}Zn_{0.45}O_{0.55}(OH)_{1.45}$ crystallite subjected to very intense electron beam bombardment. The diffraction pattern can be interpreted in terms of a composite of two phases:

(a) the $(\bar{2}\,1\,1)$ reciprocal lattice plane of a spinel phase;

(b) a hexagonal α-Fe_2O_3-related phase with the *a*-cell parameter tripled relative to the α-Fe_2O_3 (corundum-type) unit cell.*

The two phases, although in a different orientation than previously shown, are still topotactically related in the same way as the spinel and α-Fe_2O_3 lattices in Figs. 10b, c and 12; e.g. the hexagonal corundum-type *c*-axis coincides with the $[1\,\bar{1}\,\bar{1}]$ direction of the spinel phase in Fig. 13. The indices are given for selected diffraction spots of both phases. The α-Fe_2O_3-related phase is indexed on the basis of a conventional size cell and the four superstructure-type reflections are indicated by fractional indices $\{\frac{1}{3}\,0\,3\}$, $\{\frac{8}{3}\,0\,3\}$, $\{\frac{8}{3}\,0\,9\}$ and $\{\frac{1}{3}\,0\,9\}$. One can speculate that this superstructure arises from an ordering of the Zn and Fe atoms and one can consider the structure as an unstable

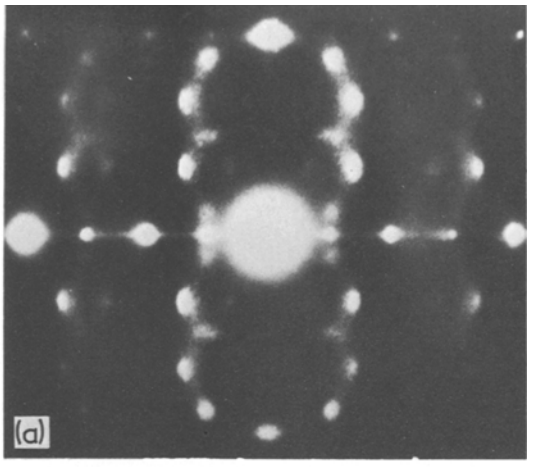

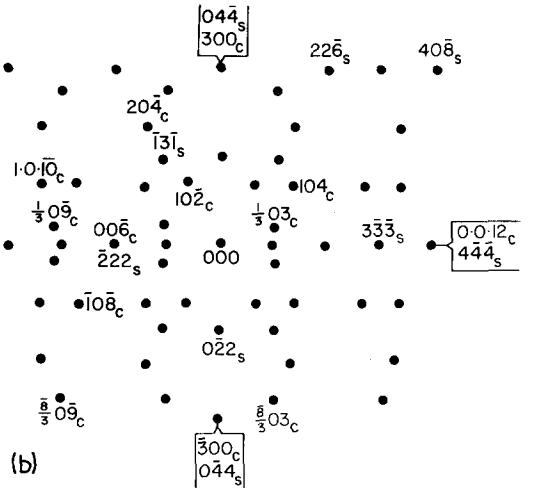

Figure 13 Electron diffraction pattern of a $Fe_{0.55}Zn_{0.45}O_{0.55}(OH)_{1.45}$ particle decomposed *in situ* under intense electron beam bombardment. Subscripts to the Miller indices refer to the two different phases: s = spinel, c = α-Fe_2O_3 or corundum-related phase.

intermediate in the decomposition process under intense electron beam bombardment. The extensive streaking in Fig. 13 is attributable to short range order; i.e. very small portions of crystal, a few atomic diameters across, have been caught in an intermediate state between the α-Fe_2O_3-related superstructure and a spinel type. The anomalously weak and diffuse nature of some spinel-type diffraction spots† points again to an incompletely developed spinel structure, with a large percentage of atoms out of place or ordered only over very small areas.

In Fig. 14, a previously undecomposed δ-type $Fe_{0.67}Zn_{0.33}O_{0.67}(OH)_{1.33}$ crystal was again

* This should be considered as a tentative interpretation.

† For example, the $\{3\,1\,1\}$ and $\{2\,2\,0\}$ spots in a well-crystallized spinel phase should be much more intense than those observed in Fig. 13.

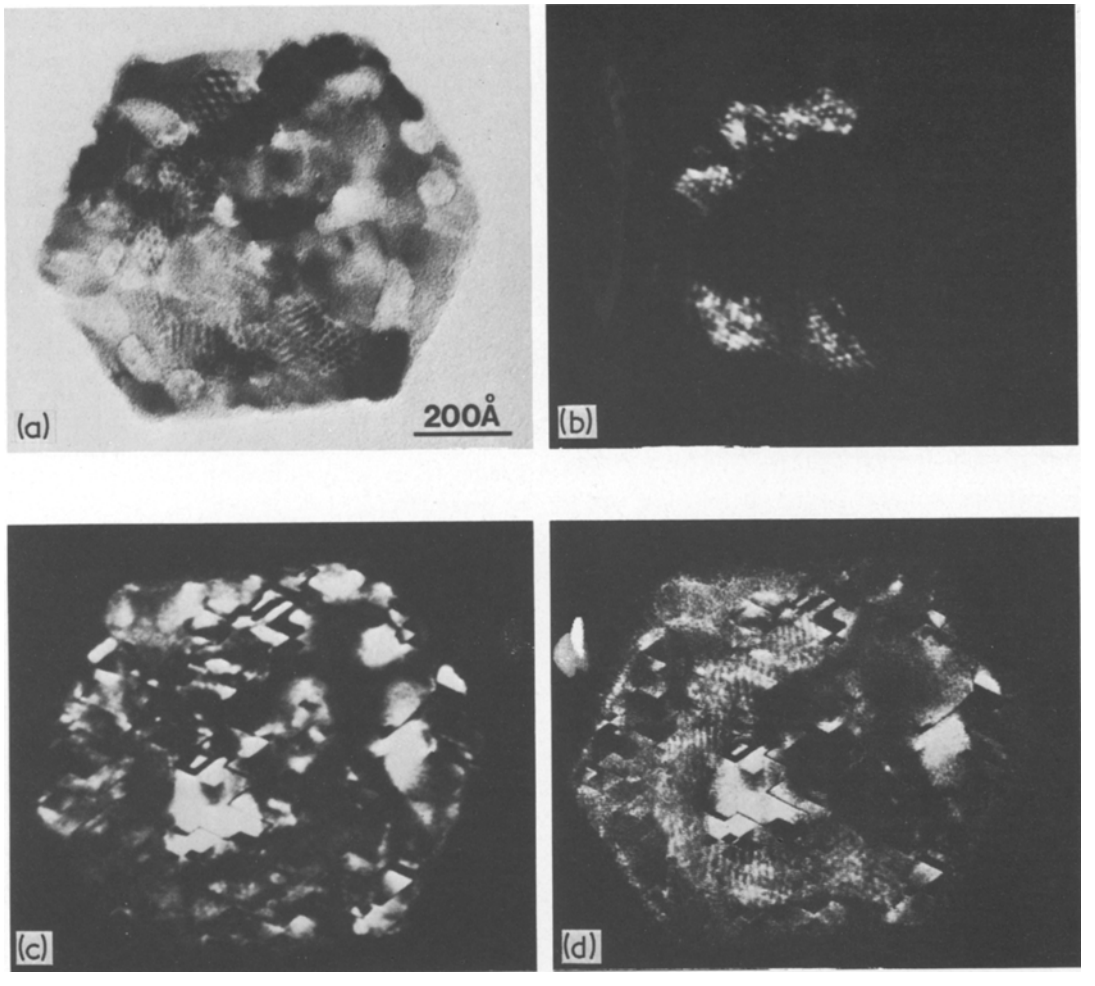

Figure 14 Bright-field (a) and dark-field (b, c, d) images of a $Fe_{0.67}Zn_{0.33}O_{0.67}(OH)_{1.33}$ particle decomposed *in situ* under intense electron beam bombardment. Aperture conditions are indicated in Fig. 15.

subjected to sufficiently intense electron beam bombardment to cause *in situ* decomposition. The resulting bright-field electron micrograph (Fig. 14a) is compared with the dark-field images (Fig. 14b, c and d) of the same crystallite obtained under the microscope objective aperture conditions shown in Fig. 15. The single-crystal electron diffraction pattern (Fig. 15) can be interpreted as a composite of (1 1 1) projections of spinel (intense hexagonal array) and the (0 0 1) of ZnO (weaker array). The pattern is similar to Fig. 12 except that the α-Fe_2O_3 (corrundum-type) pattern is missing in Fig. 15.

The most striking features of Fig. 14a are the localized moiré-type patches with spacings ~ 14 to 23 Å. Similar moiré patterns are found

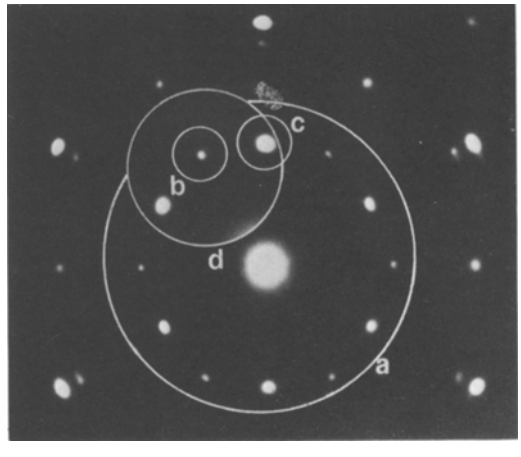

Figure 15 Electron diffraction pattern of same particle shown in Fig. 14, indicating the aperture conditions.

in Fig. 14b. As expected from Fig. 15, we note that Fig. 14d is a composite of Fig. 14b and c. The moiré pattern of Fig. 14b cannot easily be explained in terms of the aperture conditions employed (Fig. 15) since only one visible spot (the 1 0 0 of ZnO) is included. However, on close inspection of the original plate, this spot is surrounded by an array of four other extremely faint satellite spots undetectable in Fig. 15. One of these faint spots is in the position where one would expect an α-Fe_2O_3 spot (see Fig. 12). The other diffraction spots have not yet been interpreted. It appears that the moiré patterns of Fig. 14a and b can be attributed to an interaction of these satellite spots with the {1 0 0} ZnO spot. The patches of linear moirés in Fig. 14d can be interpreted as interactions between the {1 0 0} ZnO and its satellites with the neighbouring {2 2 0} spots of the spinel phase.

It is not easy to explain why these moiré patterns are so intense when some of the diffraction spots giving rise to them are almost invisible. A partial answer may lie in the localized nature of these moiré patterns. The material giving rise to the faint satellite spots is present only in a few localized areas and may be misoriented with respect to the ZnO and spinel patterns. The very weak diffraction pattern represents an average diffraction record over the whole crystal, whereas the localized moirés pinpoint those areas containing the unknown material in different orientations.

It appears that decomposition products obtained under intense electron beam bombardment (Figs. 13 to 15) are somewhat different in detail than thermally decomposed materials (Figs. 5 to 12). Unfortunately, some of these details cannot be fully elucidated, such as compositional differences in the spinel phase where a complete solid solution series exists between γ-Fe_2O_3 and $ZnFe_2O_4$ with only small differences in cell parameters [22].

3.4. The thermal decomposition of $Fe_{1-x}Ca_xO_{1-x}(OH)_{1+x}$ and $Fe_{1-x}Cd_xO_{1-x}(OH)_{1+x}$

Although the Ca- and Cd-substituted solid solutions were studied only superficially, some comments are in order. Little work was done on the Ca-substituted δ-phases due to the very limited extent of solid solution. As seen from Table I, $Fe_{0.90}Ca_{0.10}O_{0.90}(OH)_{1.10}$ decomposes in a similar fashion as the Mg-analogues with α-Fe_2O_3-type solid solutions as intermediates.

In $Fe_{1-x}Cd_xO_{1-x}(OH)_{1+x}$ phases, the decomposition scheme again resembles that of the Mg analogues with the formation of α-Fe_2O_3-type solid solutions at lower temperatures followed by exsolution of CdO and finally the formation of $CdFe_2O_4$ spinel.

The cell parameters for the Cd-substituted α-Fe_2O_3-type solid solutions are highly enlarged in the a direction due to the large ionic size of Cd^{2+}; e.g. $a_0 = 5.069$ Å, $c_0 = 13.81$ Å for $Fe_{1.90}Cd_{0.10}O_{2.95}$ made by decomposing the δ-type precursor for 5 days at 260° C. For corundum-type $Fe_{2-x}Cd_xO_{3-1/2x}$ with high Cd content the diffraction peaks are very weak and diffuse, making it especially difficult to determine accurate c_0 parameters.

References

1. M. H. FRANCOMBE and H. P. ROOKSBY, *Clay Minerals Bull.* **4** (1959) 1.
2. J. D. BERNAL, D. R. DASGUPTA and A. L. MACKAY, *ibid.* **4** (1959) 15.
3. A. L. MACKAY, Proceedings of the 4th International Symposium on Reactivity of Solids (1961) pp. 571–83.
4. S. OKAMOTO, *Kogyo Kagaku Zasshi* **67** (1964) 1850.
5. W. FEITKNECHT, *Z. Electrochem.* **63** (1959) 34.
6. A. Y. VLASOV, G. V. LOSEVA, N. V. MURASHKO and M. N. RUKOSUEV, *Izv. Vuz. Fizika* **1970** (1970) 102.
7. G. V. LOSEVA, N. V. MURASHKO, E. P. PETUKHOV, V. A. NOVITSKIY and N. V. TEPLYAKOVA, *Izvest. Akad. Nauk. SSSR Fiz. Zemli* **1975** (1975) 114.
8. G. V. LOSEVA and N. V. MURASHKO, *Inorg. Materials* **7** (1971) 1306.
9. *Idem, ibid.* **8** (1972) 423.
10. I. DEZSI, L. KESZTHELYI, D. KULGAWCZUK, B. MCINAR and N.A. EISSA, *Phys. Stat. Sol.* **22** (1967) 617.
11. A. Y. VLASOV, G. V. LOSEVA, E. F. MAKAROV, N. V. MURASHKO, E. P. PETUKHOV and V. A. POVITSKII, *Sov. Phys. Sol. Stat.* **12** (1970) 1177.
12. V. A. POVITSKII, E. F. MAKAROV, N. V. MURASHKO and A. N. SALUGIN, *Phys. Stat. Sol. (a)* **33** (1976) 783.
13. D. A. POWERS, Ph.D. Thesis, California Institute of Technology (1975).
14. W. FEITKNECHT, H. HANI and V. DVORAK, 6th Symposium on Reactivity of Solids (1968) pp. 237–45.
15. J. LIMA-DE-FARIA, *Z. Krist.* **119** (1963) 176.
16. F. DOMKA and A. BASINSKA, *Monatsh. Chem.* **110** (1979) 27.
17. F. FREUND and V. SPERLING, *Mater. Res. Bull.* **11** (1976) 621.
18. M. BLACKMAN and G. KAYE, *Proc. Phys. Soc.* **75** (1960) 364.

19. R. O. KEELING, JR. and D. A. WICK, *Science* **141** (1963) 1175.
20. P. BECKER, J. J. HEIZMANN and R. BARO, *J. Appl. Cryst.* **10** (1977) 77.
21. J. T. GRUIJTERS and G. D. RIECK, *J. Crystal Growth* **10** (1971) 207.
22. G. DUPRÉ, A. ROUSSET and P. MOLLARD, *Mater. Res. Bull* **11** (1976) 473.
23. O. MULLER, R. WILSON and W. KRAKOW, *J. Mater. Sci.* **14** (1979) 2929.
24. W. KRAKOW, H. COLIJN and O. MULLER, *ibid.* **15** (1980) 119.

Received 14 August and accepted 24 September 1979.